DOI: 10.13009/EUCASS2019-762

Experimental approach to characterize base region Coanda flow topology induced by pulsating blowing

Francisco Lozano[1], Jorge Saavedra[1], Jordan Fisher[1], Guillermo Paniagua[1], Alejandro Martinez-Cava[2] and Eusebio Valero[2]*

[1]Purdue University: Zucrow Laboratories, 500 Allison Rd, 47907 West Lafayette, IN, United States.

[2]School of Aeronautical and Space Engineering, Universidad Politecnica de Madrid

Plaza Cardenal Cisneros 3, E-28040 Madrid, Spain.

**Corresponding author: flozanov@purdue.edu*

Abstract

In the base region of airfoils, an unsteady vortex shedding occurs, which is embroiled with the compression and expansion fronts around the trailing edge. This unsteady phenomenon may be tuned using trailing edge ejection, which in turn can yield different modes of operation. These include a Coanda effect under certain flow ejection conditions. The current manuscript describes an ad-hoc experimental approach for optimal base flow region resolution. The experimental apparatus includes flush mounted Kulite sensors, pressure taps and hot wire anemometry combined with particle image velocimetry. The manuscript also reports the study of the unsteady performance of the base region under non injection conditions.

1. Introduction

The base flow region, downstream of an aerodynamic body's trailing edge, is characterized by low flow momentum and reduced pressure due to flow separation. This low momentum area is circumvented by the two families of vortices being shed from opposite sides of the aerodynamic body. The low momentum that characterizes this region is the prime contributor to aerodynamic losses, abating the aerodynamic performance. Furthermore, the unsteadiness generated by the vortices shed from the trailing edge area can promote mechanical and thermal fatigue in surrounding components. Therefore, the aft body of aerodynamic surfaces must be carefully designed [1-3]. This is a fundamental technical challenge in numerous applications for both low and high speed regimes. e.g. aircrafts, propulsion system integration, projectiles, injectors or turbomachinery airfoils.

The flow topology at the base region can be manipulated by ejecting flow at trailing edge. This is of particular interest in turbine airfoils, where coolant is exhausted at the trailing edge in order to reduce its thermal load. Ultimately, the ejected flow develops in a secondary flow stream that can be used not only for heat alleviation, but also to control the flow topology of the base region and enhance the aerodynamic performance of the airfoil. Various authors have previously addressed the particular flow physics occurring in the base region with and without flow injection via analytical, computational and experimental studies [4-7],. The effects of base bleed on vortex shedding as well as base pressure were reported. Saracoglu et al. [8-9] discovered the presence of flow bifurcations from symmetric to non-symmetric configurations at the base flow for specific ranges of blowing rates. Their findings assessed the appearance of the bifurcation for transonic and supersonic main flow conditions under certain pulsating base flow injection conditions. Above a certain blowing intensity, a difference between the pressure on both surfaces surrounding the trailing edge appears, forcing the flow to move towards one of the sides of the airfoil, disrupting the geometry of the flow field.

Copyright © 2019 by First Author and Second Author. Published by the EUCASS association with permission.

DOI: 10.13009/EUCASS2019-762

In an experimental approach, Saavedra et al. [10] analysed the effect of pulsating trailing edge blowing on the heat flux on the trailing edge vicinity for similar conditions. Martinez-Cava et al. [11] performed a deeper exploration of the physical phenomena behind the Coanda effect appearing under certain blowing intensities. These authors have performed a detailed study of a simplified trailing edge configuration combining Reynolds-averaged Navier Stokes (RANS) simulations and global stability analysis. For certain blowing intensities a symmetric base region configuration appears. While for others the vortical structures at the base region merge and lead the flow to one side, hence creating an induced Coanda effect. With the stability analysis, the authors were able to identify the global mode responsible for the change from symmetric to non-symmetric configuration, as well as its spatial structure. Additionally, Martinez-Cava et al. examined the passive flow control at the base region for two different trailing edge geometries. The first geometry consisted of a straight channel with rectangular lips, whereas the second solution integrated elliptical lips around the injection slot. The authors identified that the elliptical option further promotes the Coanda effect appearing under certain blowing conditions, hence creating larger asymmetries in the base region flow field.

Aiming a deeper understanding of the physics behind the induced Coanda effect under certain base flow injection conditions, this manuscript presents the experimental apparatus to perform high frequency measurements of the base flow region with high spatial resolution. The test section and test article are designed for enhanced resolution of the phenomena occurring at the base region. The experimental configuration enables the use of localized and optical measurement techniques, allowing simultaneous flow and surface measurements. Additionally, the first results of the base flow characterization without injection are also reported.

2. Experimental apparatus

2.1 Wind tunnel facility

The Purdue Experimental Turbine Aero-thermal Laboratory blow down linear wind tunnel was used for the experimental investigation [12], presented in Figure 1 a).). The facility relies on a 56 cubic meters reservoir of dry compressed air stored at 150 bar. Two different lines divert from the high pressure storage, the first one goes directly to the test cell and discharges the flow in a mixer. While the second line goes through a heat exchanger driven by a natural gas burner that provides non-vitiated air at higher flow temperatures. The heated supply is then combined with the cold line in the mixer. The mass flow ratio between the cold and hot lines settles the actual flow temperature. The air is then guided to the facility through a calibrated critical venturi that provides high accuracy mass flow measurements.

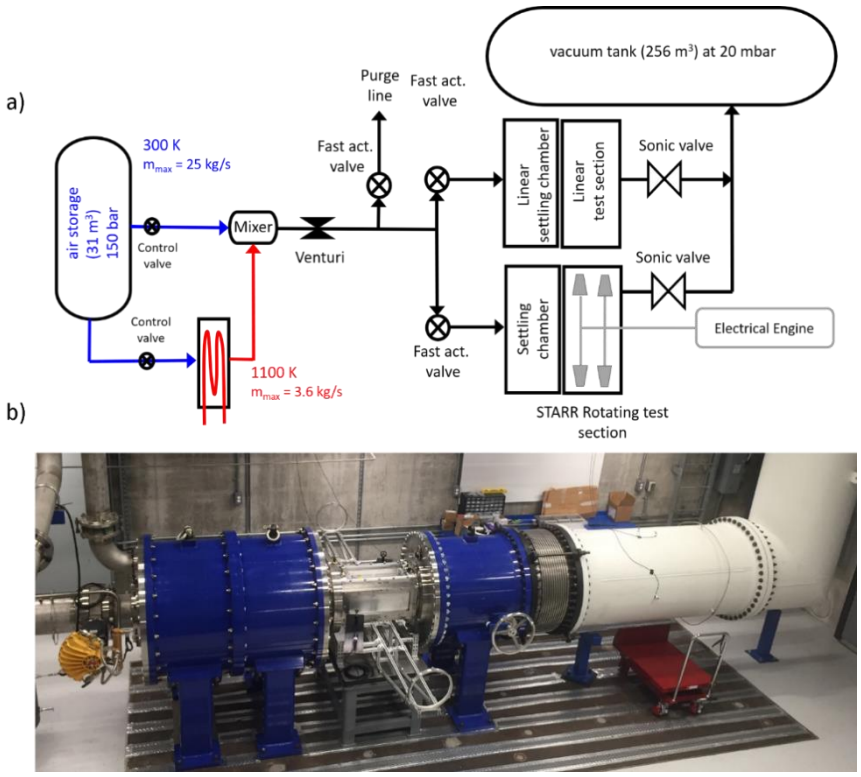

Figure 1: Wind tunnel facility; a) PETAL facility layout, b) Linear wind tunnel

DOI: 10.13009/EUCASS2019-762

During start-up procedures and while achieving uniform flow conditions the air is vented through a purge line. Once the facility operates at steady conditions the purge and test section valves are actuated, closing the purge line and guiding the flow through the linear wind tunnel, as shown in Figure 1 b). The flow enters a settling chamber, which damps the turbulence and non-axial flow disturbances, standardizing the flow conditions and guaranteeing replicability and repeatability of experiments. The axial flow leaving the flow conditioning system is delivered to the test section through an hybrid, circular to rectangular, contraction area. Finally, the flow is vented in the vacuum tank through a sonic valve. The use of the sonic valve allows the settlement of the downstream static pressure independently of the vacuum tank conditions when choked. Taking advantage of the sonic valve and varying the mass flow ratio between the cold and hot line, Reynolds and Mach numbers can be independently adjusted.

2.2 Test section for flow control experimental diagnostics

The test section for the present work was designed aiming the complete description of the physics driving the induced Coanda effect appearing under certain blowing conditions at airfoils base region. For that purpose, it was designed prioritizing three main goals:

1) Allow maximum access to base region for wall, near wall and mean flow local and global measurement techniques, including conventional and optical ones.
2) Allow passive flow control analysis through the evaluation of different geometries
3) Allow active flow control strategies implementation by flow ejection at the airfoils' trailing edge.

In order to meet the first goal, the test section was designed with three inserts on each one of the top and bottom surfaces of the test section (see Figure 2 a)). The 2 remaining sides of the test section can be either opaque surfaces when not performing optical measurements or quartz windows for complete optical resolution. The 6 inserts composing the top and bottom surfaces of the test section can be employed to accommodate instrumentation for wall and flow measurements during the different experiments. In addition, the different inserts can also accommodate windows. Therefore, the configuration of the test section designed for the present experiments is highly versatile, allowing several configurations of simultaneous flow and surface measurements.

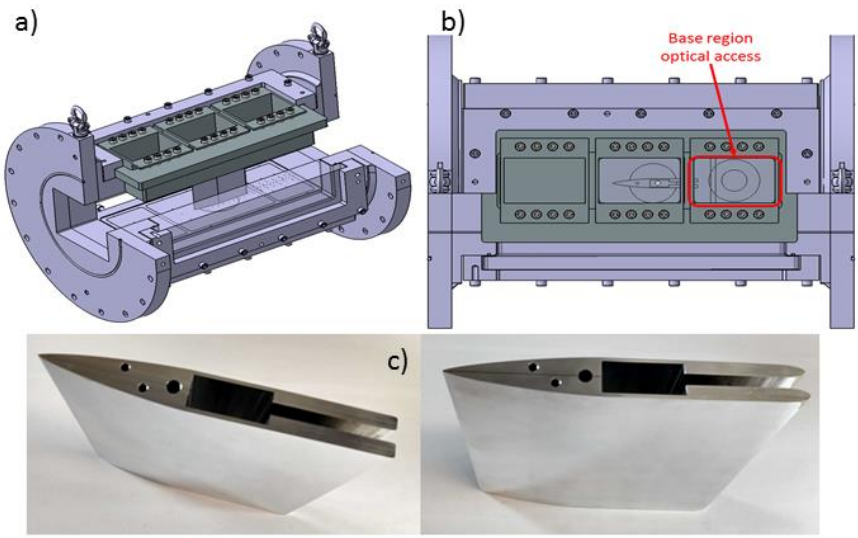

Figure 2: a) Linear test section, b) Optical access sketch, c) Airfoil models.

Furthermore, the airfoil's axial position in the test section provides 159 mm available to be instrumented with wall measurements and a maximum region of 152 mm x 101 mm that is fully accessible for optical measurement techniques downstream of the trailing edge(see Figure 2 b)). Hence, this setup enables the evaluation of wall quantities such as static pressure, mean flow quantities: total pressure, temperature, and velocity, as well as flow visualizations with techniques such as PIV.

The second goal is accomplished by the modularity of the test section's lower surface. The airfoil is attached to the working section central insert inserts, enabling the change of geometries within a few hours. For the present experimental approach, two trailing edge geometries are considered, as shown in Figure 2 c). The airfoil shape is in both cases symmetric, with a chord of 160 mm and a thickness of 20 mm at the trailing edge region. The models feature a straight (left) and an elliptic (right) shape on the lips surrounding the coolant ejection slot at the trailing edge. They

DOI: 10.13009/EUCASS2019-762

both span across the test section height, 170 mm. Both geometries were already numerically examined in the companion study performed by Martinez-Cava et al. [13].

In order to accomplish the third goal, the airfoil internal geometry and the test section integration included slots and orifices that allow the coolant flow delivery. The airfoil internal geometry features a rectangular chamber in which the desired injection pressure is delivered before the coolant goes through the ejection slot to mix with the main flow at the main region. In the test section, 2 ports for secondary lines inject flow at the cavities inside of the airfoil. Such configuration allows the flow injection in the airfoil's inner rectangular chamber from the bottom of the test section. Total pressure, total temperature and frequency of injection through these ports are independently controlled upstream of the injection point.

2.3 Instrumentation

In order to fully capture the phenomena occurring in the base region of the airfoil, this area was heavily instrumented with static pressure measurement points on the test section bottom surface. The distribution of the sensing elements is shown in Figure 3, which represents a top view of the test section bottom surface. In this image, the blue arrow labelled with U_∞ represents the main flow direction. Pressure taps were employed for low frequency pressure measurements, their location is represented by red squares while blue filled circles represent the distribution of the Kulite sensors, used for high frequency pressure measurement. The high frequency pressure transducers can capture the vortex shedding phenomena and the modifications influenced by flow injection at the trailing edge.

A total of eight Kulite sensors were used. One transducer was placed upstream of the airfoil in order to monitor any unsteadiness that might be delivered at the inlet of the test section. Two of them, one on each side of the airfoil at 48 % of the chord from the leading edge. The remaining sensors were clustered in three different axial positions: one at 7.5 %, three at 24 % and one at 38 % of the chord downstream of the trailing edge. The three Kulite sensors placed at 24 % were spaced13 mm in the pitchwise direction, placing the central one on the symmetry axis of the airfoil.

For the low frequency pressure measurements, Scanivalve sensors were employed. A total of eighty-five pressure taps are distributed along the bottom plate as depicted in Figure 3. Five of them are placed upstream of the airfoil, seven are distributed along each side of it and the rest are clustered on the base and wake region.

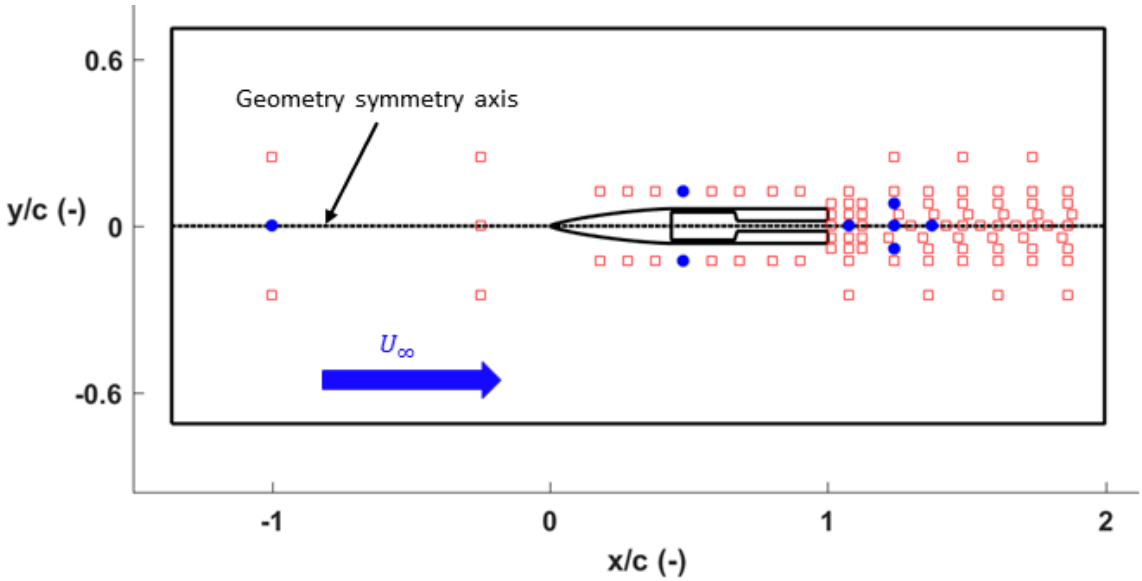

Figure 3: Wall static pressure measurement locations distribution.

The flow downstream of the airfoil was also interrogated with a hot wire anemometer. Which enabled the high frequency resolution of the fluctuations occurring in the velocity field downstream of the airfoil as well as retrieving the vortex shedding frequency. The flow is also characterized with total pressure and temperature probes upstream and downstream of the airfoil. The total pressure and temperature readings were complemented with static pressure measurements on the top surface of the test section away from the airfoil area of influence. The total to static pressure ratio upstream of the test article allows the calculation of the Mach number and flow velocity at the inlet of the test section. Hot wire measurements were also obtained at the test section inlet to retrieve the turbulent intensity and length scale, completing the description of the inlet flow conditions to the test article.

DOI: 10.13009/EUCASS2019-762

2.4 Setup for optical diagnostics

High speed Particle Image Velocimetry (PIV) was implemented in the test campaign to visualize the unsteady vortex shedding nature of the studied flow field. The design of the wind tunnel enables the use of high fidelity optical diagnostics with the incorporation of quartz windows on each side of the test section and the top of the base region. The existence of three orthonormal planes of observation allows wide camera fields of view and the delivery of large laser sheets to interrogate the test section. Previous results from numerical simulations [13] were used to select the proper measurement frequency for PIV, which was set to 10 kHz. This repetition rate was selected to be above the Nyquist criterion for the vortex shedding frequency expected for all experiments.

To achieve high-power, high frequency laser pulses, a custom burst-mode Nd:YAG laser was utilized. The fundamental 1064 nm wavelength of the laser is frequency doubled to 532 nm green light at the output of the laser for use as PIV illumination. The system is operated in a duty-cycle manner such that it can provide 10 kHz doublet pulses for 10 ms, with a cooling period of 6 seconds in between pulses. This operational mode allows for high energy pulses to be delivered for short periods of time without risking damage to the critical amplifiers in the laser.. The maximum pulse energy of the laser at 10 kHz is 150 mJ/pulse, although for this experiment the energy used is 50 mJ/pulse. The system is contained in an environmentally controlled laser laboratory adjacent to the test cell, which prevents perturbation of the laser operation due to harsh environments present during test runs. The laser beam is routed into the test cell through glass windows in the wall between the cell and laser laboratory.

The optical and camera system setup around the wind tunnel test section including the laser path is depicted in Figure 4. The laser beam lands onto an optical table adjacent to the wind tunnel test section. The optical table was fastened to the walls of the test cell for support through an optical rail/cage system which hangs above the wind. All optical equipment was vibrationally isolated from the wind tunnel to avoid misalignment of the setup during testing. After the beam lands on the optical table, it travels through a periscope so that it is aligned to mid-span of the test article. From there it travels through a +1000 mm and a – 25 mm cylindrical lens to form a wide but thin laser sheet to illuminate the probe volume. The gaussian profile of the laser sheet is expanded to a wide area so that only the brightest central portion illuminates the probe volume in a more uniform manner. The beam entered the test section through a large window installed on one of the wind tunnel's sides. The laser beam leaves the test section through another window on the opposite side, minimizing reflection and scattering issues.

To deliver seed particles to the test section, a custom built high pressure oil nebulizing seeder (Concept Smoke Vicount 5000) is used. The high temperature at the outlet of the machine causes the seed to exit as a very fine smoke which cannot be properly imaged for PIV purposes. To give the smoke time to cool and condense in larger particles the output of the seeder was fed into a small settling chamber before entering the tunnel. The residence time in the settling chamber allows control of the particle size used, and for these experiments a mean diameter of 2-3 microns was chosen. The seeder was pressurized with 100 psi (689 kPa) compressed air. For low velocity experiments this was the only source of pressure needed to deliver particles into the test section. For higher test section velocities, an extra pressure up to 200 psi (1.379×10^6 Pa) of nitrogen was supplied into the settling tank to aid the particle delivery. To encourage sufficient particle distribution and uniformity, the seeder was interfaced with the wind tunnel in the supply line upstream of the settling chamber of the tunnel. This approach improves overall seeding density and also lowers the risk of the particles causing flow disturbance since the flow is fully conditioned by the settling chamber after particles are inserted.

The camera field of view was achieved through the top window transverse to the direction of the laser beam. The third insert on the test section top was used to mount a 102x152 mm quartz window to allow for imaging directly at the trailing edge of the test article. A high speed CMOS camera (Photron SA-z) was used to capture megapixel images at 20 kHz, which capture the 10 kHz laser doublet pulses. An 85 mm lens with an aperture of f/11 was used to provide a field of view of 9.1x9.1 cm^2 and a resolution of 11.2 pixels per mm.

DOI: 10.13009/EUCASS2019-762

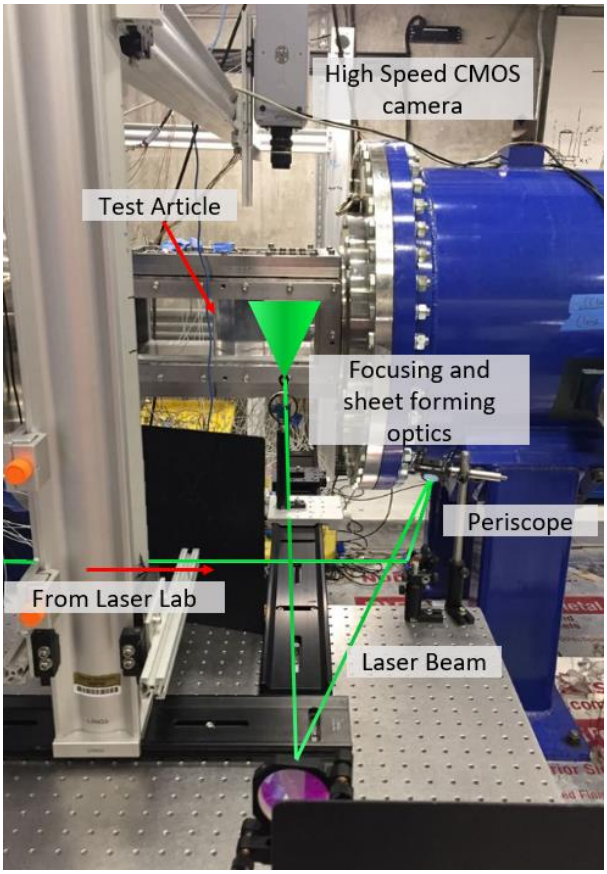

Figure 4: PIV setup showing laser beam path, test article, and camera system.

3. Experimental characterization of unaltered base flow

A first test campaign aiming at characterizing the base flow with no actuation to the airfoil model with straight trailing edge was conducted. This section of the manuscript presents the results obtained during no actuation experiments of high frequency static pressure transducers, hot wire anemometry and PIV. Five different conditions were tested. The test section inlet flow variables corresponding to each experiment are summarized in Table 1. The results reported in Table 1 are averaged in time along the measuring window for each experiment and the Reynolds number is based on the airfoil chord.

Table 1: Mean variables for the different experiments.

	Experiment 1	**Experiment 2**	**Experiment 3**	**Experiment 4**	**Experiment 5**
$Re_c\ [-]$	2.35 x 10^5	3.01 x 10^5	4.26 x 10^5	4.47 x 10^5	1.53 x 10^6
$M\ [-]$	0.06	0.08	0.11	0.18	0.34
$u\ [m/s]$	20.3	25.5	35.4	57.6	108.1
$p_0\ [Pa]$	9.98 x 10^4	10 x 10^4	10.1 x 10^4	10.3 x 10^4	11.2 x 10^4
$T_0\ [K]$	274.8	271.8	270.9	261.7	257.0

DOI: 10.13009/EUCASS2019-762

3.1 Static pressure measurements

The frequency content for the Kulite sensors depicted in Figure 3 was obtained by performing their fast Fourier transform (fft) in Matlab. The Kulite sensor closest to the inlet of the test section was taken as a reference to normalize the frequency content of each of the downstream high frequency sensors. For each frequency, the amplitude obtained from the fft for each Kulite was divided by the inlet's Kulite amplitude. This normalization isolates the base region features from any disturbance originated at the piping components or settling chamber upstream of the test section. Following this approach, the relevant unsteady phenomena associated to the airfoil performance can be clearly differentiated. The inlet frequency contents used as reference for experiments corresponding to Mach numbers 0.11, 0.18 and 0.34 are shown in Figure 5 a), b) and c), respectively.

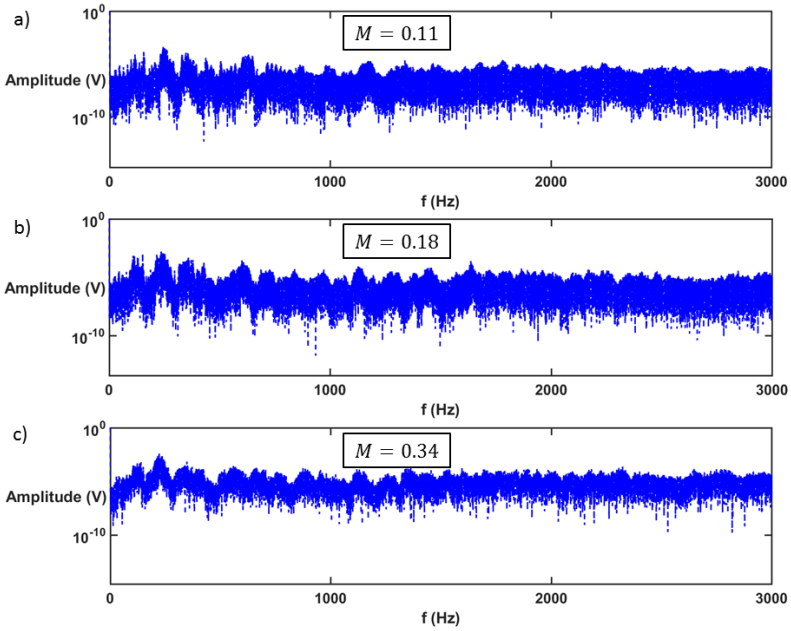

Figure 5: Inlet Kulite sensor frequency contents for experiments at Mach number: a) 0.11, b) 0.18 and c) 0.34.

Figure 6 shows the normalized frequency contents for the seven different Kulites other than the inlet ones for the experiment at Mach number 0.11. Note that in the cases in which data from more than 1 Kulite are represented, a legend identifies whether the Kulite is placed on the geometry symmetry line (center) or on the left or right of it according to Figure 3.

Figure 6 a), which corresponds to the Kulite sensors on the airfoil's sides identify two frequency peaks, one at 427 Hz and one at 568.4 Hz. These same frequencies are also retrieved in all other sensors, as depicted in Figure 6 b), c) and d). 8 % of the chord downstream of the trailing edge (see Figure 6 b)) these same peaks area also revealed without any other frequency content of a similar magnitude. Further downstream, these two frequencies appear together with other components at higher frequencies (see Figure 6 c) and d)). In all cases except for the Kulite sensor on the left of the airfoil, 427 Hz features a higher amplitude than 568.4 Hz. Hence, 427 Hz is considered the vortex shedding frequency yielded by the high frequency wall static pressure measurements for the experiment at Mach number 0.11. In Figure 6 c) a higher amplitude is observed at a frequency of 2124 Hz, which corresponds to the fifth harmonic of the vortex shedding frequency, displaying further vortex shedding amplification for this position. Figure 6 c) also shows a significantly higher amplitude in the frequency spectra corresponding to the central Kulite (red dashed line) with respect to the ones on the right and left (green das-dotted and blue dotted lines, respectively), which highlights the higher unsteadiness in the core of the wake with respect to the sides. Interestingly, the vortex shedding frequency is also perceived in upstream airfoil location, such as the Kulite sensors at ~50% of the cord. In subsonic flow conditions the acoustic disturbance generated in the base region travels upstream along the near wall region. This phenomenon is also identified in the higher Mach number experiments.

Figure 7 a) and b) show the normalized frequency content of the Kulite sensors placed 24 % of the chord downstream of the airfoil's trailing edge for the experiments at Mach numbers 0.18 and 0.34, respectively. For the experiment at Mach 0.18, the vortex shedding frequency is identified by the predominant peak at 934.7 Hz. Furthermore, a second frequency peak appears at 1941 Hz, which approximately corresponds to the second harmonic of the vortex shedding.

DOI: 10.13009/EUCASS2019-762

Figure 7 b) represents the frequency content for the highest Mach number, 0.34, where the predominant frequency which is associated with the vortex shedding appears at 2152 Hz. In this case, this frequency is surrounded by significantly lower amplitude peaks

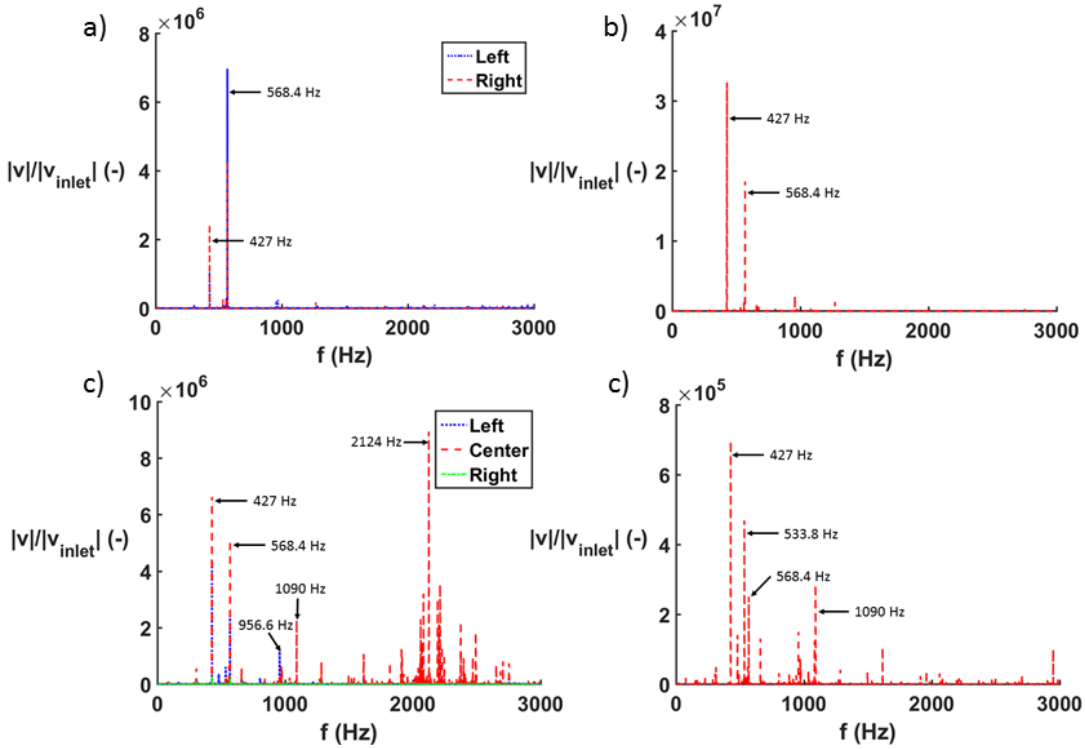

Figure 6: Normalized frequency content from Kulite sensors for the experiment at M = 0.11: a) on the airfoil's sides, b) 8 %, c) 24 % and d) 38 % of the axial chord downstream of the trailing edge.

Table *2* presents a summary of the vortex shedding frequencies identified from the high frequency wall static pressure measurements through Kulite sensors as well as the associated Strouhal numbers based on the test section inlet velocity and the airfoil's trailing edge thickness. These are reported together with the Reynolds numbers based on the airfoil's chord and the inlet Mach number for each experiment. An increase of the vortex shedding frequency can be observed when increasing the velocity (i.e. M and Re_c) of the flow as it was expected. The vortex shedding frequency obtained for the experiment with an inlet Mach number of 0.34, is close to the $2016.6\ Hz$ ($St = 0.264$) as reported by Martinez-Cava et al. [13] for the same geometry tested in this campaign with an inlet Mach number of 0.4.

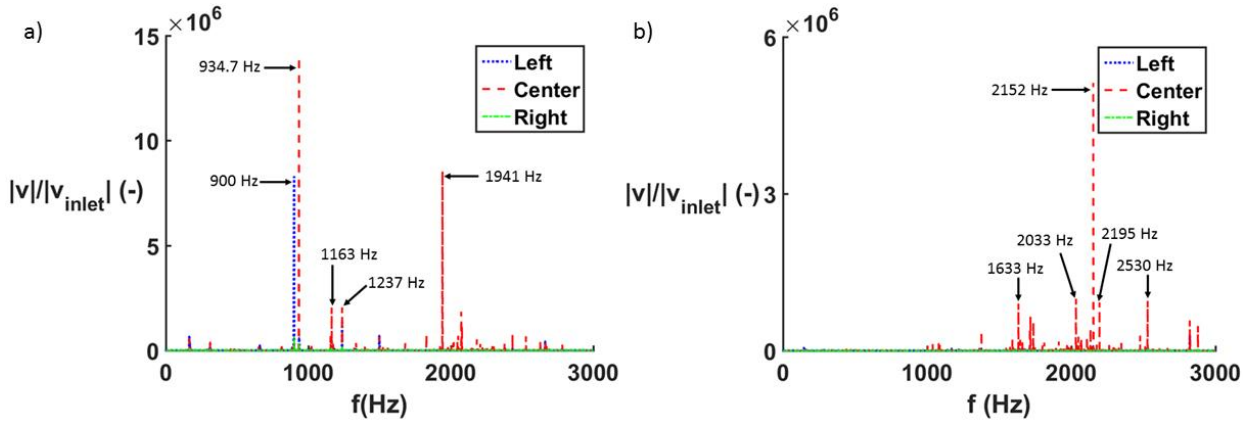

Figure 7: Normalized frequency content from Kulite sensors 24 % downstream of the trailing edge for: a) M = 0.18 and b) M = 0.34.

DOI: 10.13009/EUCASS2019-762

Table 2: Vortex shedding frequencies retrieved from high frequency wall static pressure measurements.

	Experiment 3	**Experiment 4**	**Experiment 5**
Re_c $[-]$	4.26 x 10^5	4.47 x 10^5	1.53 x 10^6
M $[-]$	0.11	0.18	0.34
Vortex shedding frequency $[Hz]$	427.0	934.7	2152.0
St $[-]$	0.241	0.325	0.398

3.2 Base flow field velocity measurements

The velocity field at the base flow was interrogated with a hot wire anemometer for the lower Mach number experiments, 0.06 and 0.08 respectively. The hot wire was placed in the mid-span plane of the test article and 0.05 chords downstream of the airfoil's trailing edge. Three different pitch wise locations were monitored, across the y-direction of the test section (see Figure 3): On the airfoil's geometry symmetry axis, $y/c = 0.16$ in negative y and $y/c = 0.16$ in positive y.

Prior to these experiments, the hot wire anemometer was calibrated in the same working section and at the relevant conditions of the experiments. The law used for these experiments was the exponential fit given by Yasa et al. [14]. Which takes into account temperature effects to increase the accuracy in flow velocity and turbulence measurements, as described in Equation 1.

$$\boldsymbol{E^2 = A + Bu^n} \tag{1}$$

During both calibration and experiments, the hot wire voltage was sampled at 115.2 kHz and low pass filtered at 55.4 kHz. Providing enough frequency range and resolution to capture the vortex shedding phenomenon, as identified by Martinez-Cava et al. [13] on CFD calculations for the same geometry studied in this test campaign. The turbulent energy spectrum for experiments at Mach numbers 0.06 and 0.08 is shown in Figure 9 and Figure 10, respectively, for the different positions of the hot wire probe. As a reference, Figure 8 shows the energy spectrum at the test section inlet for the experiments at Mach 0.06 (a) and 0.08 (b). This shows that the high noise present in the high frequency parts of the energy spectrums presented in Figure 9 and Figure 10 is not due to the airfoil's influence on the base region. It is already present at the inlet of the test section.

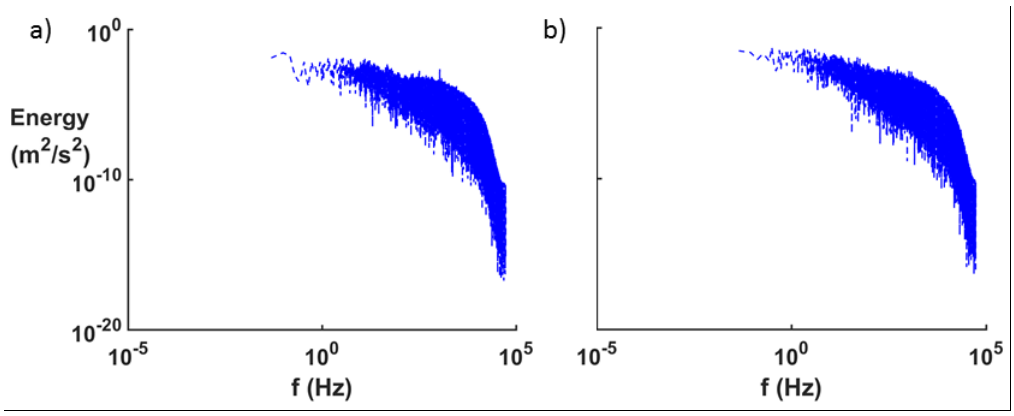

Figure 8: Inlet energy spectrum for the experiments at Mach: a) 0.06 and b) 0.08.

The hot wire measurements at y = 0 mm, airfoil symmetry plane, identify a peak frequencies of 162 and 193.8 Hz for the experiments at Mach 0.06 and 0.08, respectively. These peaks are attributed to the vortex shedding phenomenon. Additionally, those dominant frequencies are accompanied in all cases by its fourth harmonic: 638 and 801.1 Hz, respectively. When measuring out of the symmetry plane of the airfoil's geometry, this fourth harmonic has been found as well, however shifted in frequency. The vortex shedding frequencies retrieved for the experiments interrogated with hot wire anemometry and their associated Strouhal numbers (St) are reported in

DOI: 10.13009/EUCASS2019-762

Table *3* together with the test section inlet Mach number and the Reynolds number based on inlet test section conditions and airfoil's chord.

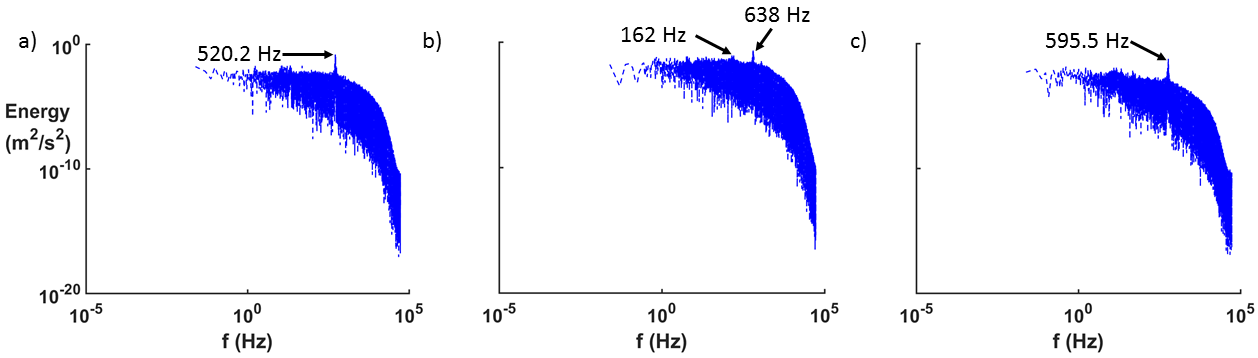

Figure 9: Turbulent energy spectrums for experiment 1 at: a) y = -25.4 mm, b) y = 0 mm and c) y = 25.4 mm.

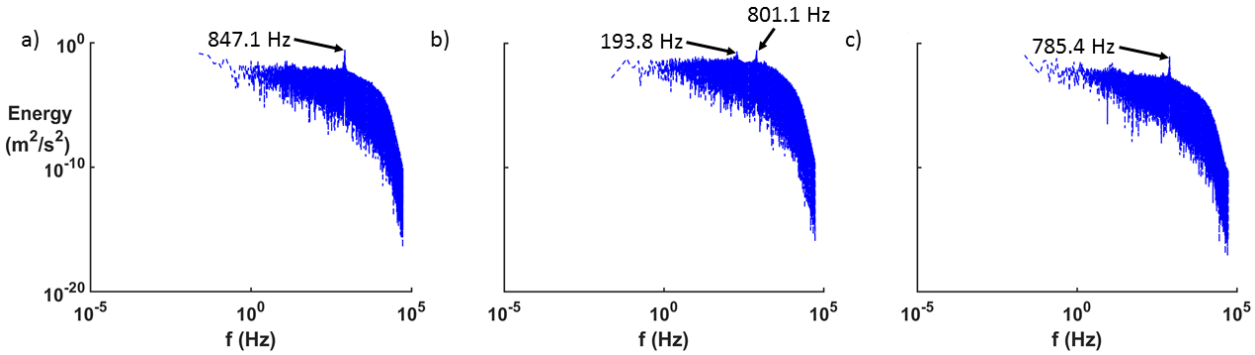

Figure 10: Turbulent energy spectrums for experiment 2 at: a) y = -25.4 mm, b) y = 0 mm and c) y = 25.4 mm.

Table 3: Vortex shedding frequencies retrieved from base region hot wire anemometry measurements.

	Experiment 1	**Experiment 2**
Re_c $[-]$	2.35 x 10^5	3.01 x 10^5
M $[-]$	0.06	0.08
Vortex shedding frequency $[Hz]$	162.0	193.8
St $[-]$	0.160	0.152

Table 4 and Table 5 present the main turbulence quantities retrieved from the hot wire anemometry measurements at the base region of the airfoil during the experiments at Mach number 0.06 and 0.08 across the three different pitch wise positions.($y/c = -0.16, 0$ and 0.16). As the mean flow velocity increases, larger mean flow velocity deficits, u_{mean}, can be perceived in the central position with respect to the other pitch-wise locations, highlighting the characteristic low momentum of the base region. The standard deviation of the axial flow velocity (u_{std}) shows significantly higher values in the center with respect to the sides as well, which correlates with the higher turbulence intensity (Tu) in the center of the geometry as well, which corresponds to the core of the wake. The dissipative length scales, (the length scales of the smallest eddies found in the base flow) have similar values for all cases, varying between 3.6 and 5.7 mm. While the integral length scale, the length scales of the largest eddies found in the base flow, are of the order of the airfoil's trailing edge thickness ($20\ mm$). Furthermore, this size has been found to increase with the velocity of the case, from $16\ mm$ for at Mach 0.06 to 23.7 at Mach 0.08. Which highlights the wake size and the base region turbulent structures size increase with higher mean flow Reynolds numbers.

DOI: 10.13009/EUCASS2019-762

Table 4: Turbulence main quantities at the base region for experiment 1.

	$\frac{y}{c} = -0.16$	$y = 0$	$\frac{y}{c} = 0.16$
u_{mean} $[m/s]$	18.31	19.25	20.58
u_{std} $[m/s]$	1.32	3.00	0.75
Tu [%]	7.40	16.09	3.70
Integral length scale $[mm]$	6.5	6.6	16.0
Dissipative length scale $[mm]$	4.4	3.6	5.7

Table 5: Turbulence main quantities at the base region for experiment 2.

	$\frac{y}{c} = -0.16$	$y = 0$	$\frac{y}{c} = 0.16$
u_{mean} $[m/s]$	27.90	23.97	27.04
u_{std} $[m/s]$	1.98	3.67	1.04
Tu [%]	7.29	15.81	3.89
Integral length scale $[mm]$	8.7	6.8	23.7
Dissipative length scale $[mm]$	4.8	3.9	5.7

3.3 Particle image velocimetry visualizations

This section details the base flow field imaging results obtained through PIV. Operations are performed in imageJ, Lavision DaVis, Matlab and Tecplot. Date were acquired for Mach numbers 0.06, 0.11 and 0.18.

3.3.1 Data Processing and Vector Creation

After raw particle images are acquired they must be put through a number of operations to reduce and transform the data to information about the velocity field. These steps include:

1) In-situ dataset quality evaluation
2) Image pre-processing
3) Vector calculation and post-processing
4) Vector conversion and data registration
5) Data post-processing and additional operations
6) Inter-dataset comparison

After all data was collected the raw images were pre-processed with ImageJ software. This consisted of a background subtraction and intensity correction so as to account for laser energy fluctuations in time. Figure 11 depicts a raw image a) together with the corresponding intensity profile b) along the yellow line in Figure 11 a). The intensity peaks correspond to identified particles.

All data sets were loaded into the PIV post-processing software (Lavision DaVis) which outputs vectors as simple pixel displacements. These were fed into Matlab, where, thanks to pre-test spatial calibrations and information on the time spacing of measurements, they were converted to velocity measurements in m/s. Using the test article coordinates, the different velocity measurements were located with respect to the geometry under study. Additional operations such as time averaging, standard deviation, vorticity and flow feature recognition were then implemented as well in Matlab.

DOI: 10.13009/EUCASS2019-762

Time-domain analysis such as Fourier transforms can also be implemented to evaluate frequency content of vortex shedding. The implementation of these processes to separated flow regimes is detailed in [15].

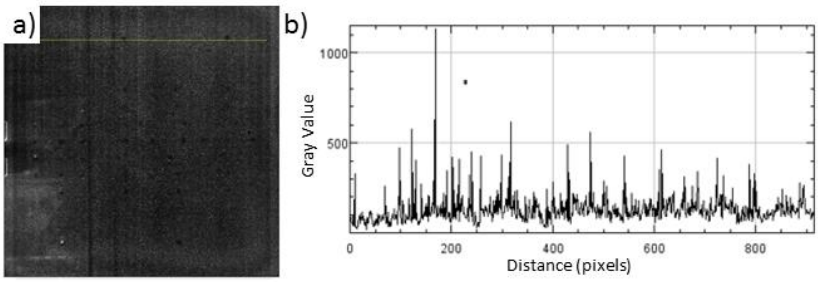

Figure 11: Raw particle image a) and corresponding intensity profile b).

3.3.2 Time-resolved flow visualizations

Initially, the time-resolved flow field for each test condition were investigated. Time series of the flow vorticity maps can be seen in Figure 12,14 and 15 for each test condition together with instantaneous velocity vectors. For the three experiments analysed, it can be observed that pockets of high vorticity depart from both sides of the trailing edge in an alternate manner. These are the vortices being shed from the point where the boundary layers from both surfaces of the airfoil detach as they arrive to the trailing edge. The vorticity values are negative for the vortices departing from the trailing edge side on the top of each map and positive for the vortices departing form the opposite side. This means that the vortices departing from the top side are rotating in the clockwise sense and the ones from the bottom do it in the opposite one, forming the von Karman vortices.

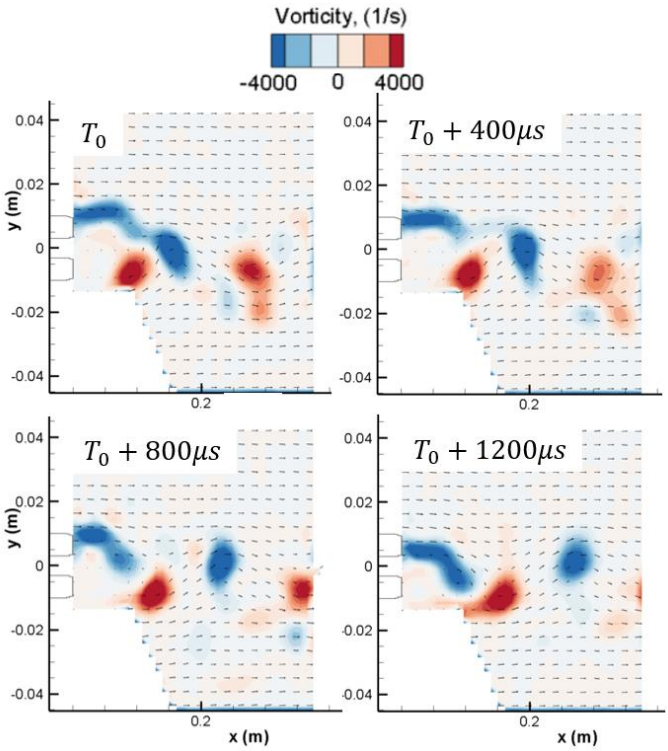

Figure 12 Time history of vortex shedding at M = 0.06.

DOI: 10.13009/EUCASS2019-762

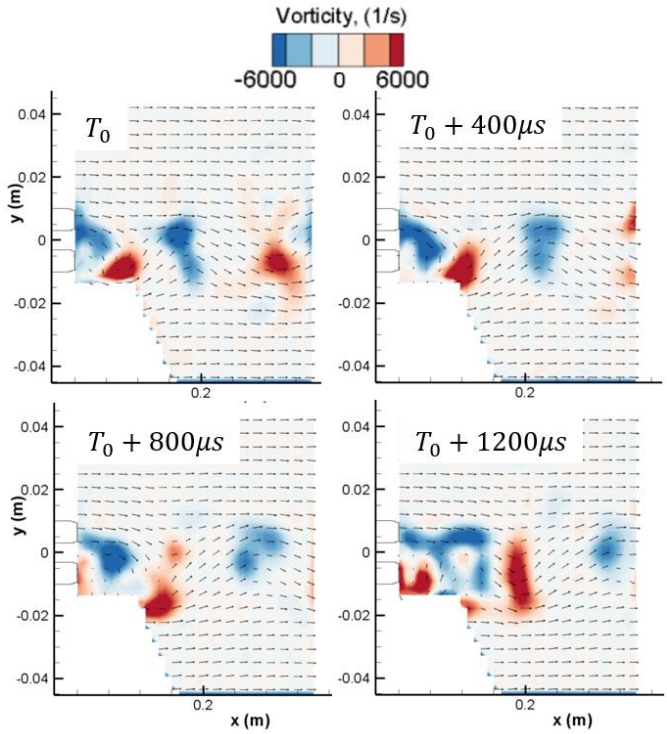

Figure 13 Time history of vortex shedding at M = 0.11.

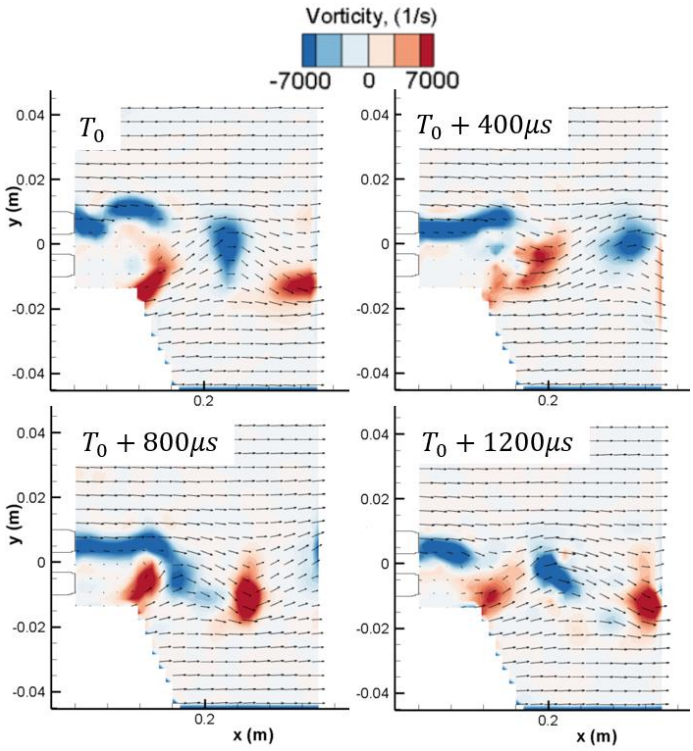

Figure 14 Time history of vortex shedding at M = 0.18.

3.3.3 Flow Field Statistics

Time-averaged results of the flow field at each explored test condition were evaluated to analyse the overall wake structure. The general base flow field topology can be seen in the time-averaged velocity maps shown in Figure 15 a), b) and c) for the experiments at Mach number 0.06, 0.11 and 0.18, respectively. Half of the base flow domain is

DOI: 10.13009/EUCASS2019-762

represented together with the corresponding half of the trailing edge geometry (black solid line on the left of each visualization). These three figures clearly show the momentum deficit of the base region, with mean velocities under 25 m/s, with respect to the outer free stream. This difference is increased as the Mach number of the main flow increases. Furthermore, the wake can be seen to be more developed as this Mach number increases as well. Accordingly, the extension of the wake increases for higher main flow velocities. The area with mean velocities under 25 m/s is observed to increase its axial length when the free stream Mach number raises, covering the full interrogated axial length for the highest velocity case explored, M = 0.18.

Figure 15 d), e), f) display the time-averaged vorticity fields at M = 0.06, 0.11 and 0.18, respectively. Areas of high vorticity can be observed at the detachment of the boundary layer and shear layer as they depart from the trailing edge and get convected downstream along the axial direction. As the Mach number of the experiments increases, the vorticity values in the shear layer become higher in absolute value. This highlights the higher intensity of the shear layer for higher Mach numbers due to the higher difference of momentum between the base region and the main flow.

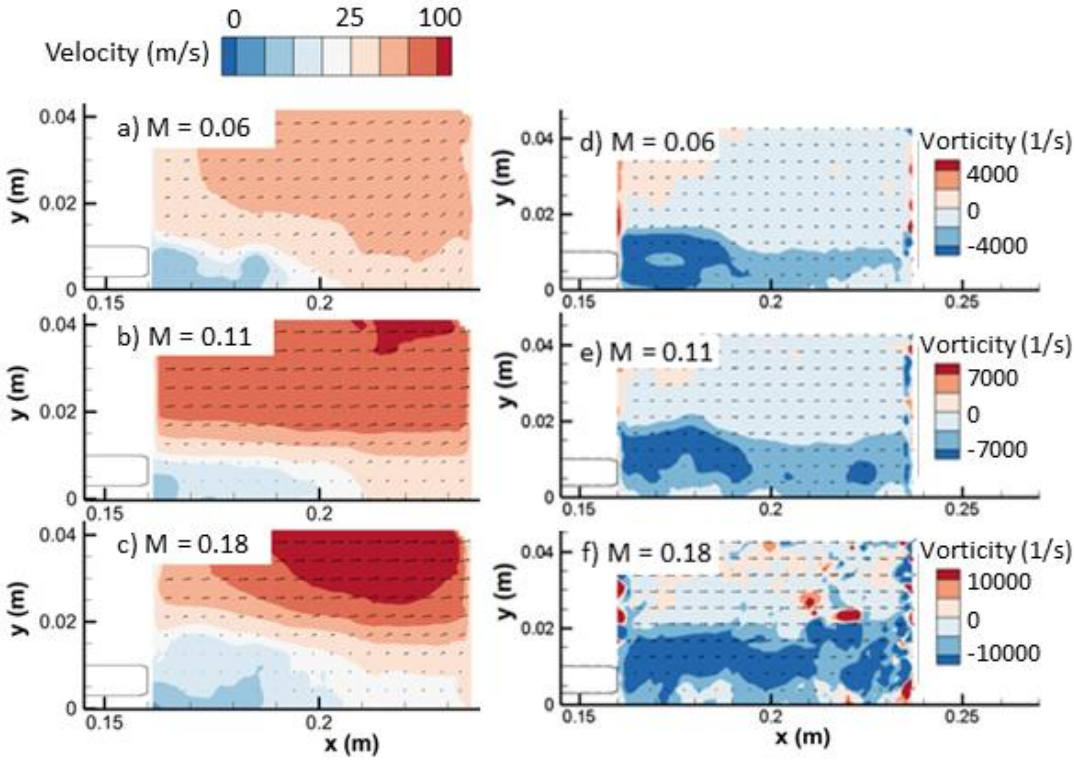

Figure 15: Standard deviation velocities a), b), and c) and average vorticity results d), e) and f), together with associated Mach numbers.

4. Conclusions

The base region and its associated unsteadiness are the prime contributor to aerodynamic losses and fatigue in a number of applications. The control of the flow physics in this area by flow injection gives the opportunity to mitigate both fatigue and induced noise. Understanding the physical mechanisms behind the base flow region unsteadiness becomes the break point towards effective and efficient flow control applications.

DOI: 10.13009/EUCASS2019-762

The design of a test section for optimal study of the base flow region unsteadiness with and without flow injection has been presented. The test article was designed aiming for large spatial resolution for both surface and mean flow measurements with combined conventional and optical measurement techniques. Particularly, the experimental apparatus presented combines the use of flush high frequency static pressure sensors, pressure taps, hot wire anemometry, and PIV. The vortex shedding phenomenon and its associated frequencies were identified for various flow conditions ranging from Mach 0.06 up to 0.34 through various measurement techniques. Additionally, the large spatial resolution allowed the characterization of the flow disturbances propagation both upstream and downstream of the base region. PIV has allowed the characterization of the base region flow topology under three different Mach number, allowing the identification of the low momentum typical of the base region as well as the two families of vortices that circumvent it.

References

[1] AGARD. 1985. Aircraft Drag Prediction and Reduction. AGARD-R-723. North Atlantic Treaty Organization.

[2] Y. Bury, T. Jardin and A. Klockner. 2013. Experimental Investigation of the Vortical Activity in the Close Wake of a Simplified Military Transport Aircraft. *Experiments in Fluids.* 54(5): 1–15.

[3] R.J. Epstein, M. Carbonaro and F. Caudron. 1994. Experimental Investigation of the Flowfield About an Unswept Afterbody. *Journal of Aircraft.* 31: 1281–1290.

[4] J.F. Nash, V.G. Quincy and J. Callinan. 1966. Experiments on Two-Dimensional Base Flow at Subsonic and Transonic Speeds. *ARC R&M.* 3427.

[5] F.R. Hama. 1968. Experimental Studies on the Lip Shock. *AIAA Journal.* 6(2).

[6] J.D. Denton and L. Xu. 1990. The Trailing Edge Loss of Transonic Turbine Blades. *Journal of Turbomachinery.* 112(2).

[7] F. Montallebi and J. Norbury. 1981. The effect of base bleed on vortex shedding and base pressure in compressible flow. *Journal of Fluid Mechanics.* 110: 273-292.

[8] B.H. Saracoglu, G. Paniagua, S. Salvadori, F. Tomasoni, S. Duni, T. Yasa and A. Miranda. 2012. Trailing edge shock modulation by pulsating coolant ejection. *Applied Thermal Engineering*. 48.

[9] B.H. Saracoglu, G. Paniagua, J. Sanchez and P. Rambaud. 2013. Effects of blunt trailing edge flow discharge in supersonic regime. *Computers and Fluids.* 88.

[10] J. Saavedra, G. Paniagua and B.H. Saracoglu. 2017. Experimental Characterization of the Vane Heat Flux Under Pulsating Trailing-Edge Blowing. *Journal of Turbomachinery.* 139(061004): 1-7.

[11] A. Martinez-Cava, Y. Wang, J. De Vicente and E. Valero. 2019. Pressure Bifurcation Phenomenon on Supersonic Blowing Trailing Edges. *AIAA Journal.* 57(1): 153-164.

[12] G. Paniagua, D. Cuadrado, J. Saavedra, V. Andreoli, T. Meyer, J.P. Solano, R. Herrero, S. Meyer and D. Lawrence. 2019. Design of the Purdue Experimental Turbine Aerothermal Laboratory for Optical and Surface Aerothermal Measurements. *Journal of Engineering for Gas Turbines and Power.* 141(012601): 1-13.

[13] A. Martinez-Cava, E. Valero, J. De Vicente and G. Paniagua. 2019. Coanda Flow Characterization on Base Bleed Configurations Using Global Stability Analysis. In: *AIAA Scitech 2019 Forum*.

[14] T. Yasa, G. Paniagua and R. Denos. 2007. Application of Hot-Wire Anemometry in a Blow-Down Turbine Facility. *Journal of Engineering for Gas Turbines and Power.* 129: 420-427.

[15] J.M. Fisher, J. Saavedra, G. Paniagua, T. R. Meyer and M.N. Slipechenko, Development of High Frequency Particle Image Velocimetry to Characterize Separation Regions Downstream of a Hump. In: *XXIV Biennial Symposium on Measuring Techniques in Turbomachinery*, Prague, Czech Republic, August 29-31, 2018.